

Half-integer Shapiro steps in highly transmissive InSb nanoflag Josephson junctions

A. Iorio,^{*,†} A. Crippa,[†] B. Turini,^{†,¶} S. Salimian,[†] M. Carrega,[‡] L. Chirulli,[†]
V. Zannier,[†] L. Sorba,[†] E. Strambini,[†] F. Giazotto,[†] and S. Heun^{*,†}

[†]*NEST, Istituto Nanoscienze-CNR and Scuola Normale Superiore, I-56127 Pisa, Italy*

[‡]*CNR-SPIN, Via Dodecaneso 33, 16146 Genova, Italy*

[¶]*Present Address: ICFO - Institut De Ciències Fotoniques, The Barcelona Institute of
Science and Technology, 08860 Castelldefels (Barcelona), Spain*

E-mail: andrea.iorio@sns.it; stefan.heun@nano.cnr.it

Abstract

We investigate a ballistic InSb nanoflag-based Josephson junction with Nb superconducting contacts. The high transparency of the superconductor-semiconductor interfaces enables the exploration of quantum transport with parallel short and long conducting channels. Under microwave irradiation, we observe half-integer Shapiro steps that are robust to temperature, suggesting their possible non-equilibrium origin. Our results demonstrate the potential of ballistic InSb nanoflags Josephson junctions as a valuable platform for understanding the physics of hybrid devices and investigating their non-equilibrium dynamics.

The advancing quantum technologies have made the investigation of low-dimensional hybrid superconducting nanostructures a major area of research in recent years. When a normal conductor is coupled to a superconductor, the superconducting correlations can penetrate into the non-superconducting region through the proximity effect.^{1,2} As a result,

the hybrid system can exhibit unique properties derived from both the normal and superconducting components, offering exciting possibilities for novel functionalities. This phenomenon has been investigated in various solid-state platforms, including semiconductors,^{3,4} two-dimensional electron systems,⁵⁻⁷ magnetic and ferroelectric materials^{8,9} and topological insulators.¹⁰⁻¹² In this context, Indium Antimonide (InSb) is a particularly promising semiconductor, known for its high electron mobility, narrow bandgap, strong Rashba spin-orbit coupling, and large g^* -factor.^{7,13-16} Due to the challenges of growing InSb quantum wells on insulating substrates, free-standing InSb nanoflags have emerged as a highly flexible platform, as they can be grown without defects on lattice-mismatched substrates.¹⁷⁻²⁸ They have also been referred to as nanoflakes, nanosheets, or nanosails in the literature.^{18-20,29} Recently, InSb nanoflags have been used to realize proximity-induced superconductor-normal metal-superconductor (SNS) Josephson junctions, which exhibit ballistic and gate-tunable supercurrents,^{21,30,31} clear subharmonic gap structures,^{22,30} and non-local and non-reciprocal supercurrent transport.^{19,31} These developments highlight the potential of InSb nanoflags as a platform for exploring the complex dynamics between charge, spin, and superconducting correlations, including topological superconductivity,^{32,33} gate-tunable hybrid superconducting qubits,³⁴⁻³⁶ and non-equilibrium quasiparticle dynamics.³⁶⁻³⁸

In this work, we present a thorough investigation of highly transmissive ballistic Josephson junctions on InSb nanoflags made with niobium (Nb) contacts. Compared to previous works,^{30,31} our device has a higher junction transparency, which enables the investigation of unexplored transport regimes. Our findings reveal the coexistence of parallel short and long conducting channels, as confirmed by the temperature dependence of the critical current and magnetoresistance. Under microwave irradiation, we observe Shapiro steps at half-integer values of the canonical voltage $hf/2e$, which exhibit a non-monotonic evolution with temperature. The observation suggests that a non-equilibrium state is formed in the junction due to the microwave drive.

The device depicted in Figure 1a and 1b consists of a planar SNS junction made of an InSb

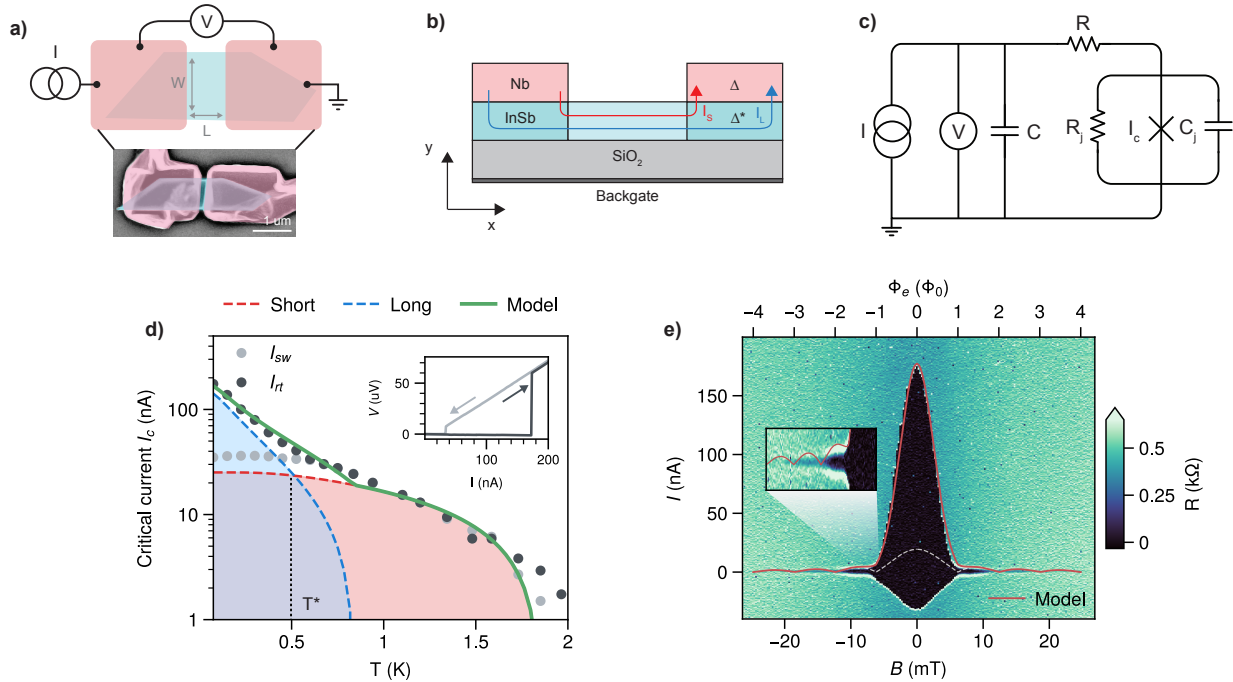


Figure 1: (a) Upper part: sketch of the sample with the relevant dimensions and a simplified measurement setup. The junction length is $L = 80$ nm and the width is $W = 650$ nm. Lower part: scanning electron micrograph of the SNS junction. The InSb nanoflag has a trapezoidal shape, and the Nb contacts are patterned on top of it. (b) Schematic cross-section of the device, where the superconducting Nb contacts with gap Δ proximitize an induced gap Δ^* in the InSb layer.³⁹ The red and blue lines represent, respectively, the short and long conducting channels that are discussed in (d). (c) Extended RCSJ model, with the Josephson junction of critical current I_c in parallel with a shunt resistance R_j and capacitance C_j . Additional shunt capacitance C and resistor R take into account the dissipative environment around the junction. (d) Temperature dependence of the switching current I_{sw} (black dots) and the retrapping current I_{rt} (grey dots). The blue and red areas indicate the contributions of the long and short conducting channels, respectively, as estimated from the corresponding models. The green line represents the sum of the two contributions. Inset: forward (black line) and backward (grey line) current sweeps used to extract the switching I_{sw} and retrapping I_{rt} currents, respectively. (e) Differential resistance $R = dV/dI$ plotted as a function of the bias current I and the out-of-plane magnetic field B . The red curve takes into account both the long and short model contributions. The grey line shows the Fraunhofer pattern resulting from the short channel only. The inset provides a zoomed-in view of lobes in the low-bias region.

nanoflag with two Nb contacts. Previous studies have revealed that these InSb nanoflags are defect-free and exhibit a zincblende structure with high mobility (up to $29\,500\text{ cm V}^{-2}\text{ s}^{-1}$) and a mean free path $l_e \simeq 500\text{ nm}$ at 4.2 K .²⁸ The Fermi wavelength $\lambda_F \simeq 30\text{ nm}$ for a carrier concentration of $n_s \simeq 8.5 \times 10^{11}\text{ cm}^{-2}$ is comparable to the thickness of the nanoflags ($\simeq 100\text{ nm}$), resulting in a strong quasi two-dimensional character. Measurements were performed using a standard four-wire technique at the base temperature of $T = 75\text{ mK}$ of a dilution refrigerator. A highly doped Si backgate allows for control of the carrier density of the InSb and was set to $V_G = 40\text{ V}$ for the results shown in the following. Microwave signals are applied via an open-ended attenuated coaxial cable placed $\sim 1\text{ cm}$ away from the chip surface. The junction dynamics is modeled using an extended resistively and capacitively shunted junction (RCSJ) model, which takes into account the dissipative environment surrounding the junction, as depicted in Fig. 1c.^{3,40,41} Further information on materials, fabrication, and measurement techniques can be found in the Supporting Information.

We first characterize the device in the absence of microwave irradiation. A typical back and forth sweep $V(I)$ is presented in the inset of Figure 1d, in which a current bias I is applied and the resulting voltage drop V across the junction is measured. The $V(I)$ characteristics shows a considerable hysteresis with a switching current $I_{sw} \simeq 170\text{ nA}$ and a retrapping current $I_{rt} \simeq 30\text{ nA}$. The hysteresis in planar SNS junctions is commonly due to electronic heating in the normal region,⁴² with a finite junction capacitance C_j potentially contributing¹.

Figure 1d shows the temperature dependence of the switching and retrapping currents on a semi-log scale. We can distinguish two distinct regions in the data. For temperatures $T > T^*$, with $T^* \sim 500\text{ mK}$ (see Figure 1d), the switching current follows the predictions of a short junction model (shown as a red shaded area). However, for $T \leq T^*$, we see a deviation from the short junction behavior, and the switching current follows an exponential increase with decreasing T , which is characteristic of long junctions (blue shaded area). The

¹In our device, the geometric junction capacitance is estimated $\sim \text{aF}$, which may not cause a noticeable hysteresis, but intrinsic capacitance effects cannot be ruled out.⁴³⁻⁴⁵

data can be well-reproduced over the entire temperature range using a simple model that considers the transport predominantly determined by two conducting channels, long and short, as illustrated in Figure 1b and demonstrated by the green line in Figure 1d.

In the short junction limit $L \ll \xi_N$ (where $\xi_N = \hbar v_F / \Delta \simeq 720$ nm is the coherence length, with $v_F \simeq 1.5 \times 10^6$ m/s²⁸ and $\Delta \simeq 1.35$ meV), the supercurrent flows directly through the InSb region between the Nb contacts separated by $L = 80$ nm. For simplicity, we assume that all modes in the junction have equal effective transmission τ , which can be described in the ballistic limit ($L \ll l_e$) by:⁴⁶

$$I_S(T) = \max_{\varphi} \frac{\bar{N} e \Delta^{*2}(T)}{2\hbar} \frac{\tau \sin \varphi}{E_A(\varphi, T)} \tanh \frac{E_A(\varphi, T)}{2k_B T}, \quad (1)$$

with \bar{N} the number of effective modes, $E_A(\varphi, T) = \Delta^*(T) \sqrt{1 - \tau \sin^2(\varphi/2)}$ the Andreev bound state (ABS) energy of the mode, $\Delta^*(T) = \Delta^*(0) \tanh \left(1.74 \sqrt{T_c/T - 1} \right)$ the temperature-dependent induced energy gap,²⁴⁷ and φ the macroscopic phase-difference across the junction. The best fit with the short junction model yields the red dashed line in Figure 1d, with a single mode $\bar{N} = 1$, $\tau = 0.93$ and $T_c = 1.85$ K, and a value of critical current $I_S = 25$ nA at $T = 75$ mK. The observed lower values of currents are consistent with the transport mechanism illustrated in Fig. 1b, where the supercurrent flows between the two proximized InSb regions with an induced gap Δ^* , rather than being dominated by the Nb gap Δ .

The exponentially enhanced conduction at low temperatures is typical of long channel states (of length d). The conduction via these states holds in the long junction limit $d \gg \xi_N$, and reads:⁴⁸

$$I_L(T) = \frac{E_{Th}}{R_N e} a \left[1 - 1.3 \exp \left(-\frac{a E_{Th}}{3.2 k_B T} \right) \right], \quad (2)$$

where $E_{Th} = \hbar v_F l_e / 2d^2$ is the Thouless energy,² R_N is the junction resistance and $a = 3$.³ The best fit of the long junction model is shown as the blue dashed line in Figure 1d and

²We are assuming for simplicity a BCS gap.

³The constant a is dependent on the ratio E_{Th}/Δ^* .⁴⁸

yields $E_{Th} \sim 20 \mu\text{eV}$, corresponding to $d \sim 3.5 \mu\text{m}$, close to the total length of the InSb nanoflag ($3.35 \mu\text{m}$), $R_N \sim 400 \Omega$ and a critical current $I_L \sim 140 \text{ nA}$ at $T = 75 \text{ mK}$.

Previous studies have documented similar results in highly transmissive ballistic SNS junctions with topological insulators or graphene,^{4,49–54} with the behavior being attributed to contributions from both surface and bulk states.^{51,53} One study linked the low-temperature enhancement to a low-energy Andreev bound state localized around the circumference of the junction.⁵⁰ In our nanoflags, this could be consistent with electronic transport at the edges of the nanoflag due to band-bending, similarly to what has been reported by de Vries et al.¹⁹. Compared to earlier works on InSb nanoflags that employed a Ti sticking layer between Nb and InSb,^{30,31} the increase of I_{sw} at low temperature is consistent with the increased transparency achieved in this study through the direct deposition of bare Nb on the passivated surface of InSb, without the use of additional metallic layers.

Magnetotransport measurements further confirm the coexistence and magnitude of the two current conducting channels in the junction, providing additional insight into the current density distribution across the channels. The differential resistance of the junction $R = dV/dI$ as a function of magnetic flux is presented in Figure 1e. An unconventional Fraunhofer pattern, with a first lobe much more pronounced than the side lobes, is visible and well-described by the superposition of a conventional Fraunhofer pattern typical of short junctions, and a monotonic quasi-Gaussian decay, which is characteristic of long SNS junctions.^{52,55–59} The forward-biasing of the current results in a non-symmetrical supercurrent region for switching and retrapping currents (black area). The periodicity of the Fraunhofer pattern corresponds to one flux quantum inside the junction, taking into account a London penetration depth of $\lambda_L \simeq 100 \text{ nm}$ ⁶⁰ and a flux enhancement of a factor of $\Gamma_f \sim 1.8$ due to flux focusing within the planar geometry. The critical current values from short and long transport channels estimated in Figure 1d are used here to model the magnetic interference patterns. The red line in Figure 1e shows the combined contribution of both channels to the supercurrent $I(\Phi_e) = I_S(\Phi_e) + I_L(\Phi_e)$, where $\Phi_e = \Gamma_f B(L + 2\lambda_L)W$ is the applied magnetic

flux on the uncovered junction area, with $W = 650$ nm the junction width. The standard Fraunhofer pattern $I_S(\Phi_e) = I_S |\sin(\pi(\Phi_e/\Phi_0))/(\pi\Phi_e/\Phi_0)|$ expected for a wide-short junction, and a Gaussian decay $I_L(\Phi_e) = I_L \exp(-\sigma\Phi_e^2/\Phi_0^2)$, typical of a narrow-long junction, are accounted for in the calculation. We have included a possible different effective area of the long junction directly in the estimated value of $\sigma \sim 0.329$ while preserving the same flux dependence.

Our conclusions are further supported by the temperature-dependent change in the magnetoresistance, which exhibits an exponential reduction of the Gaussian component and limited variation in the Fraunhofer lobes up to $T = 800$ mK (refer to Figure S3 of the Supporting Information). The lack of distinct oscillations in the magnetoresistance indicates that possible edge states are not interfering coherently with magnetic fields perpendicular to the nanoflag. However, the impact of flux screening, phase decoherence, and transport along various facets of the flag make it challenging to arrive at more definitive conclusions.

Having established the response of the junction at equilibrium, we will now examine how the system behaves when subjected to a microwave irradiation. In Figure 2a, we present a sample $V(I)$ curve with a microwave tone at frequency $f = 1.75$ GHz and applied power $P_{RF} = 12$ dBm. As it can be difficult to estimate the precise power delivered to the sample, we will only refer to the power provided by the signal generator in the following discussion. Quantized voltage steps of amplitude $n \times hf/2e$ appear in the $V(I)$ characteristic (black line), as a result of the phase-locking between the microwave frequency and the junction Josephson frequency.⁶¹ In addition to integer steps occurring at $n = \pm 1, \pm 2, \pm 3, \dots$, half-integer steps appear with $n = \pm 1/2, \pm 3/2, \pm 5/2, \dots$. The overlapping grey trace displays dV/dI and shows peaks associated to both integer and half-integer steps, some of which are highlighted by red arrows. Steps with fractions different from multiples of $1/2$ are not observed. A histogram, resulting from the binning of the voltage data, is shown on the left and provides an immediate visual representation of the length of each step. The bin unit equals the current step size, such that the number of counts corresponds to the width of the

voltage plateaus.

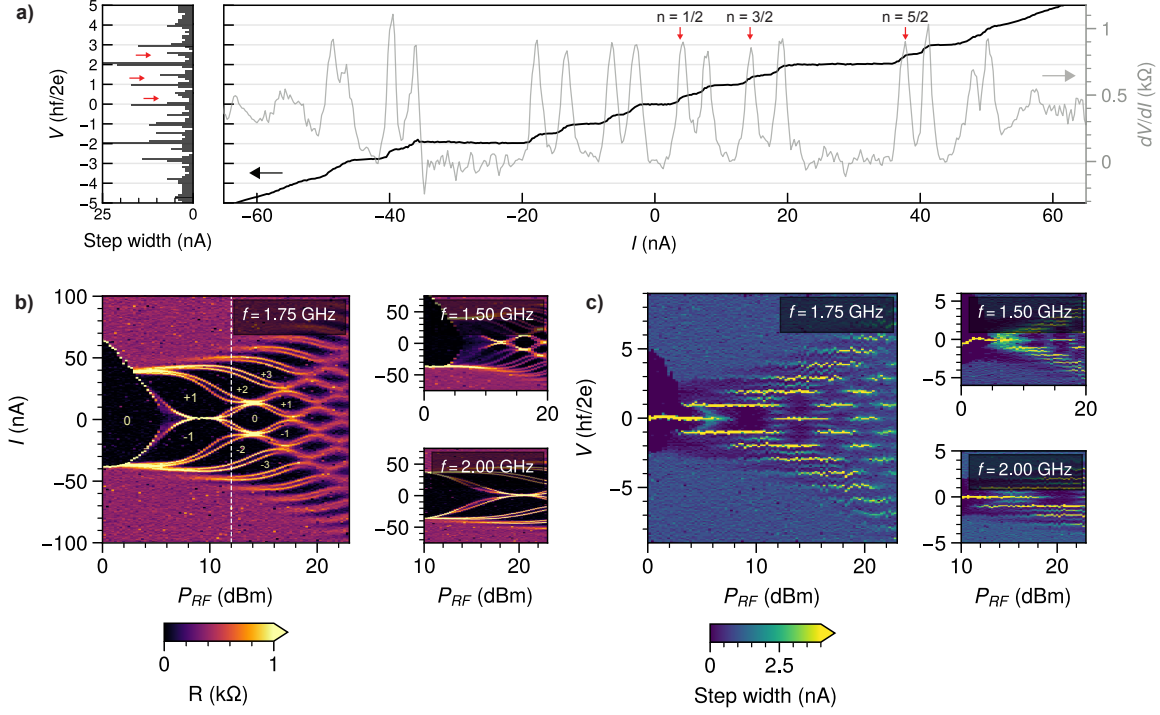


Figure 2: (a) Sample $V(I)$ curve (black) in the presence of microwave irradiation at $P_{RF} = 12$ dBm and frequency $f = 1.75$ GHz. The grey line represents the differential resistance $R = dV/dI$ with arrows highlighting half-integer Shapiro steps. The histogram on the left shows the distribution of the voltage data. The bin unit is equal to the current step size, such that the number of counts corresponds to the width of the voltage plateaus. The value of P_{RF} refers to the one provided by the signal generator. (b) Full evolution of R as a function of current bias I and microwave power P_{RF} at $f = 1.75$ GHz. Pairs of bright peaks indicate the presence of half-integer steps. The white dashed line corresponds to the data shown in (a). Label numbers refer to the corresponding step index n . The right side shows the colormaps for $f = 1.50$ GHz and $f = 2.00$ GHz. (c) Histograms, as shown in (a), are displayed based on the data in (b) in a colorplot as a function of microwave power P_{RF} .

Figure 2b shows a color plot of R as a function of I and P_{RF} . Sharp jumps in voltage appear as bright peaks in R , while voltage plateaus corresponds to dark regions. The pattern of bright peak pairs in the data provides stark evidence of fractional steps that occur over a wide range of power and frequencies, as demonstrated by the maps at $f = 1.50$ GHz and $f = 2.00$ GHz. The region between the plateaus ± 1 displays bistability at around $P_{RF} = 10$ dBm of applied power, with sudden switching occurring between the two overlapping plateaus (see the Supporting Information for additional discussion). Figure 2c better

highlights the emergence of Shapiro steps by depicting the evolution of the histogram data as a function of microwave power for various frequencies. In the Supporting Information, we present additional measurements for different backgate voltages, magnetic field values, and temperatures.

We then study the behavior of the system by increasing the temperature. Figure 3a displays Shapiro maps at temperatures ranging from $T = 75 \text{ mK}$ ($\sim 0.02 \Delta^*/k_B$) to $T = 1.5 \text{ K}$ ($\sim 0.5 \Delta^*/k_B$). The temperature rise leads to a decrease of the supercurrent and an increase in thermal fluctuations, resulting in rounded voltage plateaus. However, the half-integer steps remain stable from base temperature up to around 1 K ($\sim 0.3 \Delta^*/k_B$), where the current-phase relationship (CPR) given by the equilibrium supercurrent is expected to be mostly sinusoidal (as illustrated in Figure S10).

Figure 3b shows the change in step width for the steps $n = 0$ and $n = 1/2$ extracted from Figure 3a. The amplitude of the integer step decreases monotonically with increasing temperature, while the half-integer step shows a non-monotonic trend, with a maximum at $T \simeq 400 \text{ mK} \sim 0.12 \Delta^*/k_B$. This is also demonstrated in Figure 3c, where the step widths for $n = 0, 1$ and $n = 1/2, 3/2$ are plotted on a semi-log scale as a function of T . While the integer steps show an exponential decrease, the width of the half-integer steps first increases, then decreases, and eventually saturates due to the noise level at high temperatures. This remarkable evolution points to a non-equilibrium origin of the half-integer steps and is consistent with predictions and experimental observations that non-equilibrium supercurrents are less rapidly impacted by temperature compared to equilibrium supercurrents, which are suppressed exponentially.^{5,62–66}

In the Supporting Information, we provide data from an additional device with lower transparency. While the junction behaves similarly under microwave irradiation, the signatures of the half-integer steps are considerably weaker.

Despite their frequent occurrence, the origin of fractional steps in superconducting devices is not univocal. Measurements of fractional Shapiro step are commonly used to identify

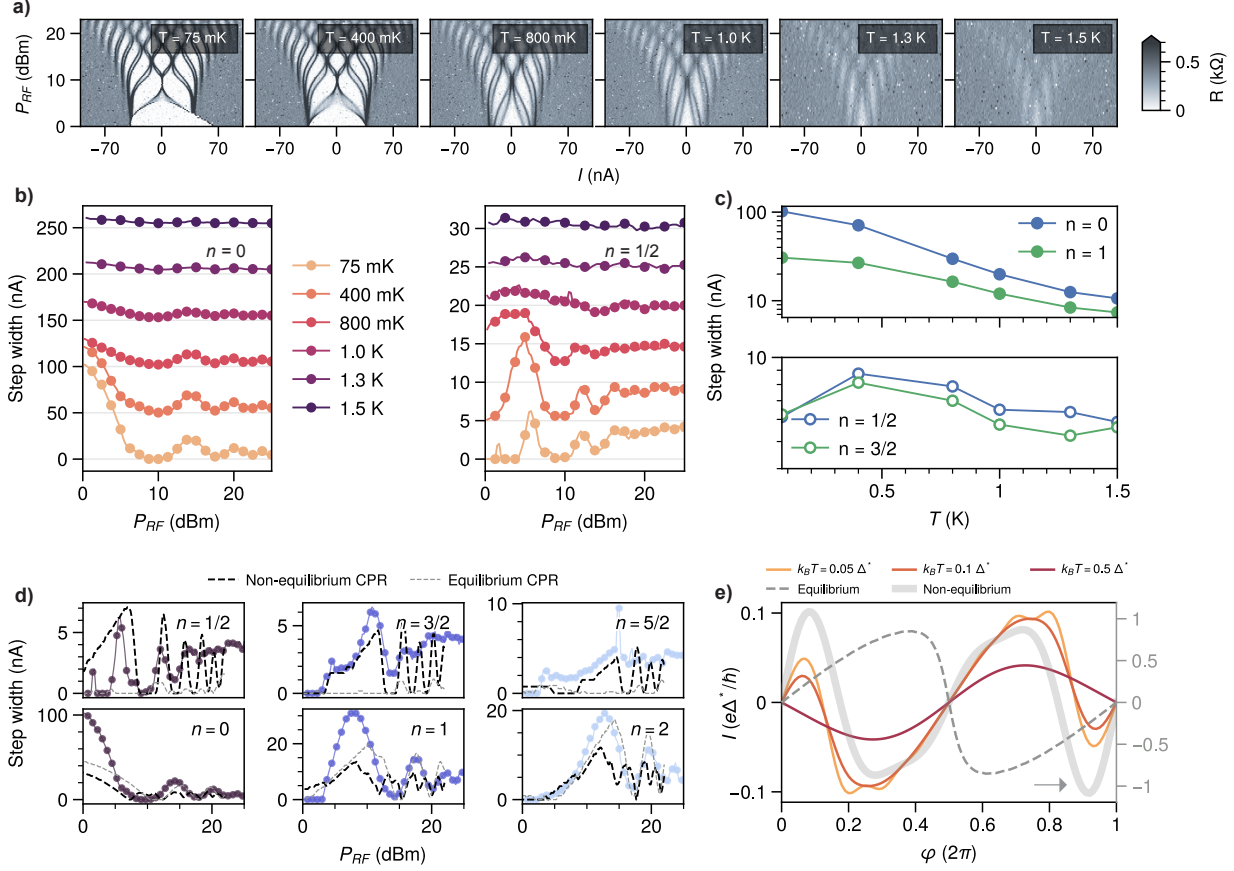


Figure 3: (a) Shapiro maps at different temperatures $T = (75$ mK, 400 mK, 800 mK, 1.0 K, 1.3 K, 1.5 K) at $f = 1.75$ GHz. (b) Step width for $n = 0$ (left) and $n = 1/2$ (right) extracted from the temperature maps show in (a). As temperature increases, a monotonic decrease is observed for $n = 0$, while a non-monotonic evolution with a maximum at 400 mK is observed for $n = 1/2$. Traces are offset for clarity, with an offset of 50 nA (left) and 5 nA (right). (c) Step widths displayed on a semi-log scale as a function of T for integers $n = 0, 1$ (top) and half-integers $n = 1/2, 3/2$ (bottom). Microwave powers $P_{RF} = 0$ dBm for $n = 0$, $P_{RF} = 8$ dBm for $n = 1$, $P_{RF} = 5.5$ dBm for $n = 1/2$, and $P_{RF} = 11$ dBm for $n = 3/2$. (d) Step width of half-integer $n = 1/2, 3/2, 5/2$ (top) and integer $n = 0, 1, 2$ (bottom). Each trace is a horizontal slice of Figure 2c. The dashed black lines represent the numerical simulations obtained from the extended RCSJ model using the non-equilibrium CPR shown as the thick grey line in (e). The dashed grey lines represent the simulations using the equilibrium CPR. (e) CPRs under microwave irradiation for $\tau = 0.98$ and driving $w = 1.3$ at different temperatures ($k_B T = 0.05, 0.1$, and $0.5 \Delta^*$) are depicted by light to dark orange lines. The dashed grey line represents the equilibrium CPR at $w = 0$ and $k_B T = 0.05 \Delta^*$, for the same value of τ . The thick grey line represents the effective non-equilibrium CPR used in panel (d).

non-sinusoidal CPRs in highly transparent SNS junctions,⁶⁷ or in junctions incorporating ferromagnetic layers^{8,9,68,69} or those exhibiting exotic superconducting states.^{70,71} Geometric or intrinsic capacitance,^{43–45,57,72} and circuit feedback^{40,73,74} can also contribute to the appearance of fractional steps or hysteretic behavior. Sub-harmonic structures may also indicate a unique mode of a more complex circuit network, as seen in junction arrays^{75–80} and superconducting quantum interference devices (SQUIDs).^{77,81,82} These manifestations are also visible even in the absence of multiple superconducting terminals, as in grain boundary or step-edge junctions,^{83–86} as a consequence of the complex evolution of multiple phase-locked states.

The fractional steps reported in the previous examples, including both ballistic and diffusive SNS junctions, are ascribed to the equilibrium properties of the supercurrent and can be understood within a phenomenological extended resistively and capacitively shunted junction (RCSJ) model, which takes into account the dissipative environment surrounding the junction, as depicted in Fig. 1c.^{3,40,41} In the phase-particle picture, neglecting capacitive effects, the phase evolves in a washboard potential that is tilted by the applied bias current and modulated by the time-dependent drive. Shapiro steps arise as time-dependent phase slips between the minima of the Josephson potential, and for a typical $\sin(\varphi)$ CPR, integer steps arise as $2\pi n$ phase slips. Within this picture, half-integer Shapiro steps require an energy-phase relation that displays a secondary minimum and arise when the second harmonic of the CPR is stronger than the first one.

However, a microwave drive can also significantly alter the supercurrent's steady-state behavior.^{5,37,62–66,87–94} The adiabatic changes in the ABS energies, as well as the multiple transitions induced by microwave photons between the ABSs or between the ABSs and the continuum, can result in a non-trivial dynamics of the supercurrent-carrying states.^{62,90,92,93} Such effects can give rise to highly distorted CPRs, which exhibit sign-reversals of the supercurrent and π -periodic oscillations at twice the Josephson frequency.^{5,63,64,87,89,91,95}

We notice that in the experiment the induced gap $\Delta^* \simeq 280 \mu\text{eV}$ (67 GHz), so that we

cover values $hf \simeq 0.03 \Delta^*$. In an effort to capture the emergence of half-integer Shapiro steps, we describe the junction dynamics by adiabatically incorporating non-equilibrium effects into the RCSJ model of Fig. 1c through a single effective CPR. The latter is provided by the thick grey line in Fig. 3e, and its origin will be discussed later. In Figure 3d, we plot the step width for integer and half-integer values of n vs. P_{RF} , obtained as horizontal slices of Figure 2c at constant V . The dashed black line in the figure shows the results of the simulation using the effective non-equilibrium CPR, while the dashed grey line represents the equilibrium one. Although the equilibrium CPR effectively reproduces the integer steps in the oscillatory pattern (bottom row), it completely fails to capture the half-integer steps (top row). This is despite the presence of higher-order harmonics in the highly skewed CPR, which are often attributed to the origin of half-integer steps.⁶⁷

To gain further insight into the origin of such a distorted CPR, we used a tight-binding method within the Keldysh-Green's function approach^{90,93} to numerically calculate the current-phase relationship of an SNS junction irradiated by a microwave tone. The model describes a single-channel Josephson junction with an arbitrary junction transparency τ and gap Δ^* . The microwave driving is included as a time-dependent modulation of the phase difference across the junction with amplitude $w = eV_{RF}/hf$. Figure 3e shows the simulated CPR for microwave irradiation of $hf = 0.1 \Delta^*$ at a microwave driving of $w \sim 1.3$ and $\tau = 0.98$ for different temperatures. The dashed grey line represents the equilibrium CPR. The microwave irradiation significantly alters the CPR, boosting a strong second harmonic, which results in the development of an additional minimum. This provides insight into the origin of the effective non-equilibrium CPR used in the RCSJ model. The wiggles in the CPR are due to non-equilibrium population of Floquet sidebands produced by the microwave driving and disappear at temperatures on the order of the driving frequency, $k_B T \sim hf$. In turn, the secondary minimum is robust and still visible at $k_B T = 0.1 \Delta^*$, as shown in Figure 3e, and it qualitatively agrees with the robustness of the half-integer steps with respect to temperature. In the Supporting Information, we detail the theoretical model

and present additional simulations showing that reducing the junction transparency results in the disappearance of the CPR's secondary minimum (Figure S10).

The outlined procedure should be regarded as an attempt to reconcile the results of the adiabatic approximation, typical of the RCSJ model, with the microscopically calculated CPR in the presence of microwave driving and in the absence of a steady voltage across the junction. In particular, the model reproduces the two-minima shape of the effective non-equilibrium CPR only within a limited range of w values, which is inconsistent with the experimental observations and highlights the limitations of the present description. Alternative phenomenological theories of non-equilibrium supercurrents have been proposed,^{5,63,87} which model the system by considering both the ABSs and their occupation distributions oscillating at the Josephson frequency. The specific structure of the ABSs, including the effects of finite junction length or ballistic quasi two-dimensional transport, may be responsible for the discrepancies between different predictions, which calls for more comprehensive theories.

In conclusion, we have investigated a highly transmissive Josephson junction made of an InSb nanoflag with Nb contacts. Our results indicate strong evidence of parallel transport in both long and short conducting channels, confirmed by the temperature-dependent supercurrent and magnetic field interference. Under microwave irradiation, we observe strong half-integer Shapiro steps, showing a non-monotonic temperature evolution that points to non-equilibrium effects induced by the driving. The observed phenomenology is only partially captured by the predictions based on the adiabatic approximation in terms of a non-equilibrium CPR. Further theoretical developments are needed to address the presence of strong second harmonic supercurrents in ballistic, highly transparent SNS junctions. Future experiments should investigate the potential of InSb nanoflag Josephson junctions for exploring the coherent manipulation of Andreev states and their non-equilibrium dynamics.

Acknowledgement

The authors thank Daniele Ercolani for his help with the growth of the InSb nanoflags and Michal Nowak for useful discussions. This research activity was partially supported by the FET-OPEN project AndQC (H2020 Grant No. 828948). E.S. and F.G. acknowledge the EU's Horizon 2020 research and innovation program under Grant Agreement No. 800923 (SUPERTED) and No. 964398 (SUPERGATE) for partial financial support.

Supporting Information Available

Sample Information and Measurement Techniques

The InSb nanoflags utilized in this work have been extensively described in previous studies.^{23,28} They are defect-free structures that exhibit excellent electrical properties, including high mobility (up to $29\,500\text{ cm V}^{-2}\text{ s}^{-1}$) and a large mean free path ($l_e \simeq 500\text{ nm}$) at $T = 4.2\text{ K}$. The devices were fabricated by placing nanoflags on a p -doped Si/SiO₂ substrate, which serves as a backgate, and connecting them with 150 nm of Nb. A passivation step was performed prior to metal deposition to improve the semiconductor-metal transparency. Further information on device fabrication can be found in the supporting material of Salimian et al.³⁰, Turini et al.³¹. We conducted transport measurements using a low-temperature Leiden Cryogenics dilution refrigerator with a base temperature of 75 mK. The cryostat is equipped with a three-level filtering system, comprising π filters at room temperature as well as cryogenic π and RC filters at base temperature. The $V(I)$ curves were acquired in a standard four-wire configuration, with the junction current-biased using a Yokogawa GS200 voltage source over a 10 M Ω resistor. The voltage drop over the junction was amplified by a factor 1000 using a room temperature DL1201 voltage preamplifier operated in battery mode and acquired by an Agilent 34410 multimeter. We applied voltage to the backgate using a Keithley 2602 voltage source. Microwave signals were applied using an R&S SMR20

microwave source to an attenuated semi-rigid open-ended coaxial cable in close proximity to the sample holder, which had been attenuated by 20 dB and 10 dB at 3K and Cold plates, respectively. For measurements in magnetic field, we used a low-noise Keithley 2400 sourcemeter connected to a 2 T American Magnetics magnet.

Dependence on Backgate Voltage

Figure S1(a-d) displays $V(I)$ curves in a higher current range at different backgate voltages V_G ranging from 10 V to 40 V. The black dashed line fitted to the Ohmic region allows obtaining the normal state resistance R_N and excess current I_{exc} . In panel (e), we present the switching current I_{sw} and retrapping current I_{rt} over the same range of gate voltages. The switching current I_{sw} decreases from 170 nA to 75 nA as the gate voltage is varied, while the retrapping current I_{rt} remains roughly constant at approximately 30 nA.

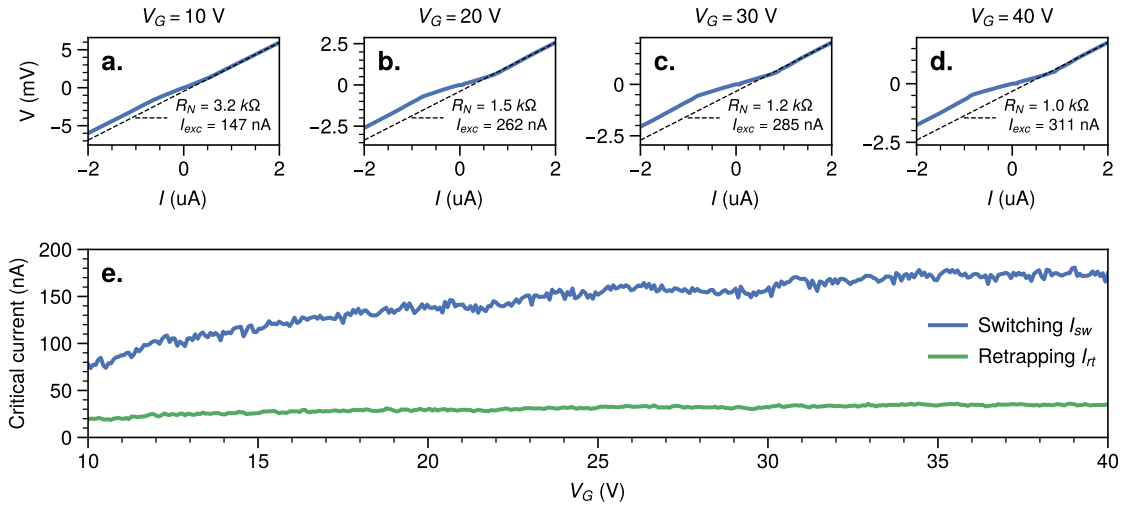


Figure S1: (a-d) Sample I-V traces for different V_G values (10,20,30,40) V. The black dashed line is the linear fit to the Ohmic region used to extract R_N and I_{exc} . (e) Full backgate dependence of the switching and retrapping current in the same gate voltage range.

Figure S2a depicts the evolution of R_N and $G_N = 1/R_N$ as a function of V_G , with the resistance decreasing from 3 $k\Omega$ (at $V_G = 10$ V) to 1 $k\Omega$ (at $V_G = 40$ V). Figure S2b shows the excess current as a function of V_G in the same range. The product $I_{exc}R_N$ remains

roughly constant at about $350 \mu\text{V}$ ($1.2 \Delta^*/e$) over the entire gate voltage range, close to the theoretical value of $8/3 \Delta^*/e$ predicted for the ballistic case (Fig. S2c).⁹⁶ Moreover, the product $I_{sw}R_N$ is expected to be $I_{sw}R_N = 10.82 E_{Th}/e$ for a long diffusive junction in the limit $\Delta^* \gg E_{Th}$.⁴⁸ In our device, $I_{sw}R_N$ varies from $180 \mu\text{V}$ to $250 \mu\text{V}$ ($7 - 10 E_{Th}/e$) (Fig. S2d).

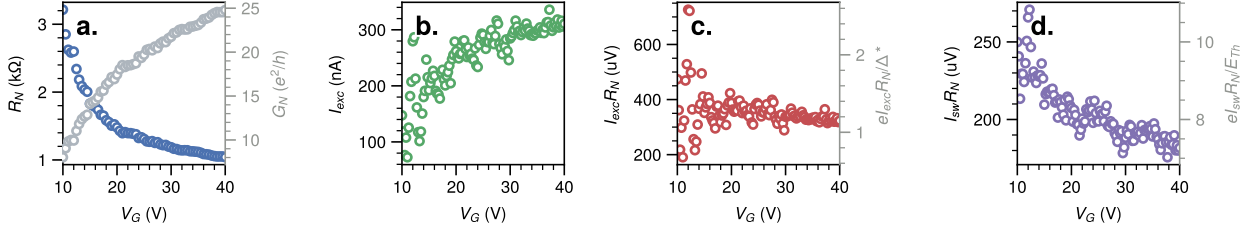


Figure S2: (a) Normal state resistance R_N , (b) excess current I_{exc} , (c) $I_{exc}R_N$ product, and (d) $I_{sw}R_N$ product plotted as functions of the backgate voltage V_G .

Magnetic Interference Maps

Figures S3 and S4 present additional measurements of magnetic interference patterns at different temperatures, $T = (300, 500, 800)$ mK, and backgate voltages, $V_G = (30, 20, 10)$ V. The magnetoresistance maps in Figure S3 demonstrate a decrease in the Gaussian-like contribution as the temperature increases, further confirming that the exponential suppression of I_{sw} is related to states in the long junction limit. The Fraunhofer diffraction side-lobes remain unchanged up to a temperature of 500 mK, consistent with the limited dependence of $I_{sw}(T)$ for modes in the short junction limit, and eventually begin to disappear only for $T > 800$ mK.

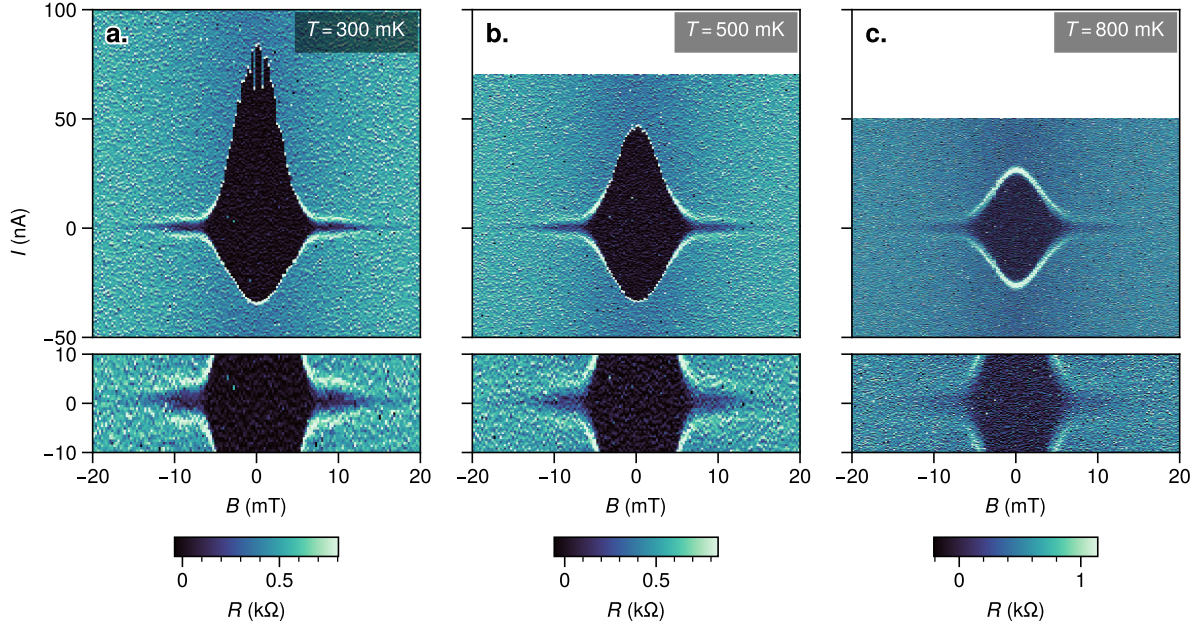


Figure S3: Magnetoresistance maps at temperatures of (a) 300 mK, (b) 500 mK, and (c) 800 mK. Below each panel, a zoom-in on the low bias region shows the behavior of the side-lobes with respect to T .

Figure S4 shows the magnetoresistance evolution in V_G . States in the long junction limit are more sensitive to changes in the semiconductor depletion level at low gate voltages V_G , as evidenced by the corresponding changes in the Gaussian amplitude. Only a little variation of the Fraunhofer diffraction lobes is observed confirming the high homogeneity of the current density in the short junction area between the electrodes.

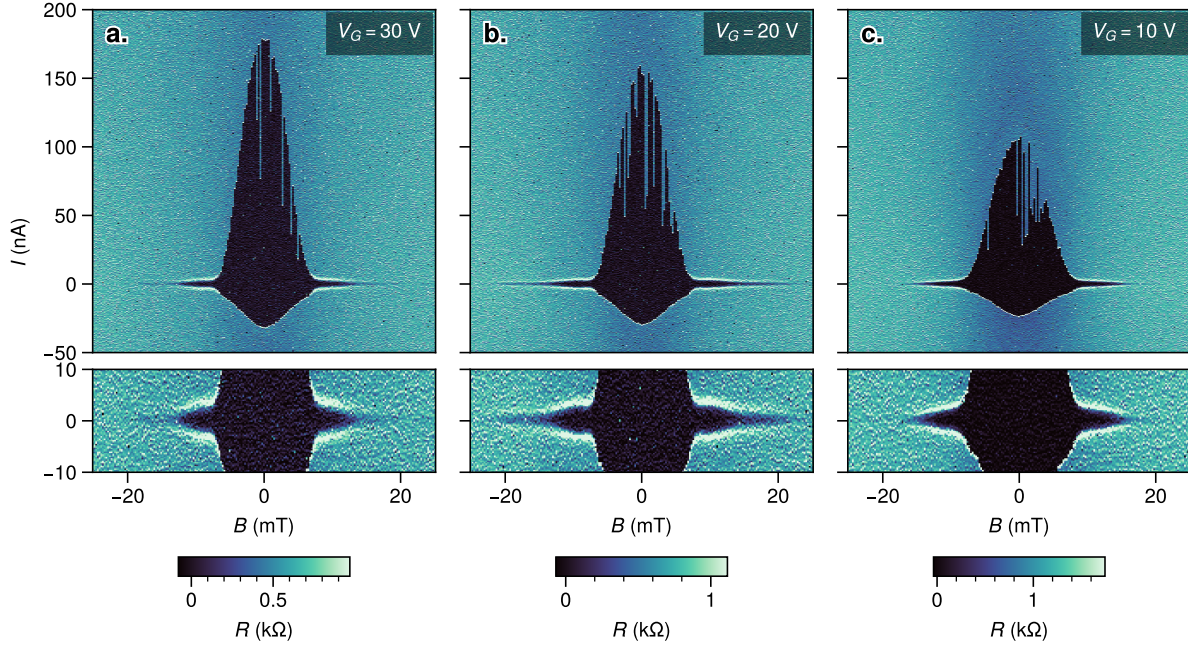


Figure S4: Magnetoconductance maps at backgate voltage V_G of (a) 30 V, (b) 20 V, and (c) 10 V. Below each panel, a zoom-in on the low bias region shows the behavior of the side-lobes with respect to V_G .

Shapiro Maps at finite Magnetic Field

Figure S5 depicts the Shapiro maps obtained at a frequency of $f = 1.75$ GHz for different out-of-plane magnetic field values ranging from 0 to 11 mT. As the magnetic field suppresses I_c , the reduced drive frequency $\Omega = \frac{2\pi f}{2eI_c R_j / \hbar}$ increases, and the $V(I)$ maps follow the Bessel function dependence on the applied RF power.^{40,41}

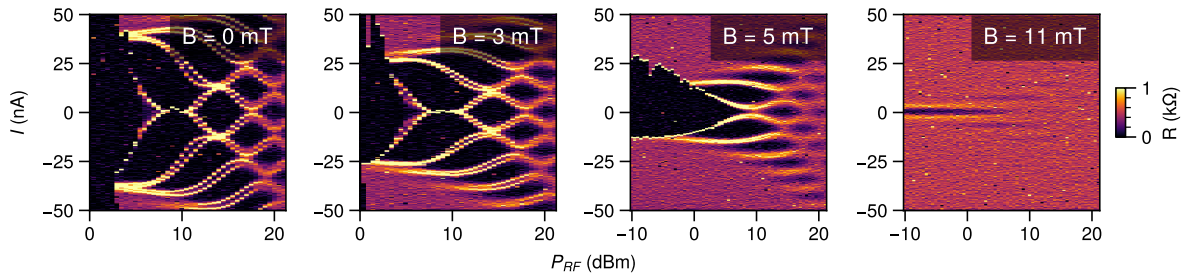


Figure S5: Shapiro maps at $f = 1.75$ GHz for various out-of-plane magnetic field strengths B ranging from 0 to 11 mT.

Shapiro Maps at different Backgate Voltages and Temperatures

The evolution of the half-integer steps is robust in temperature and backgate voltage, as detailed by the scans in Fig. S6 for $V_G = 40$ V (top row) and $V_G = 10$ V (bottom row).

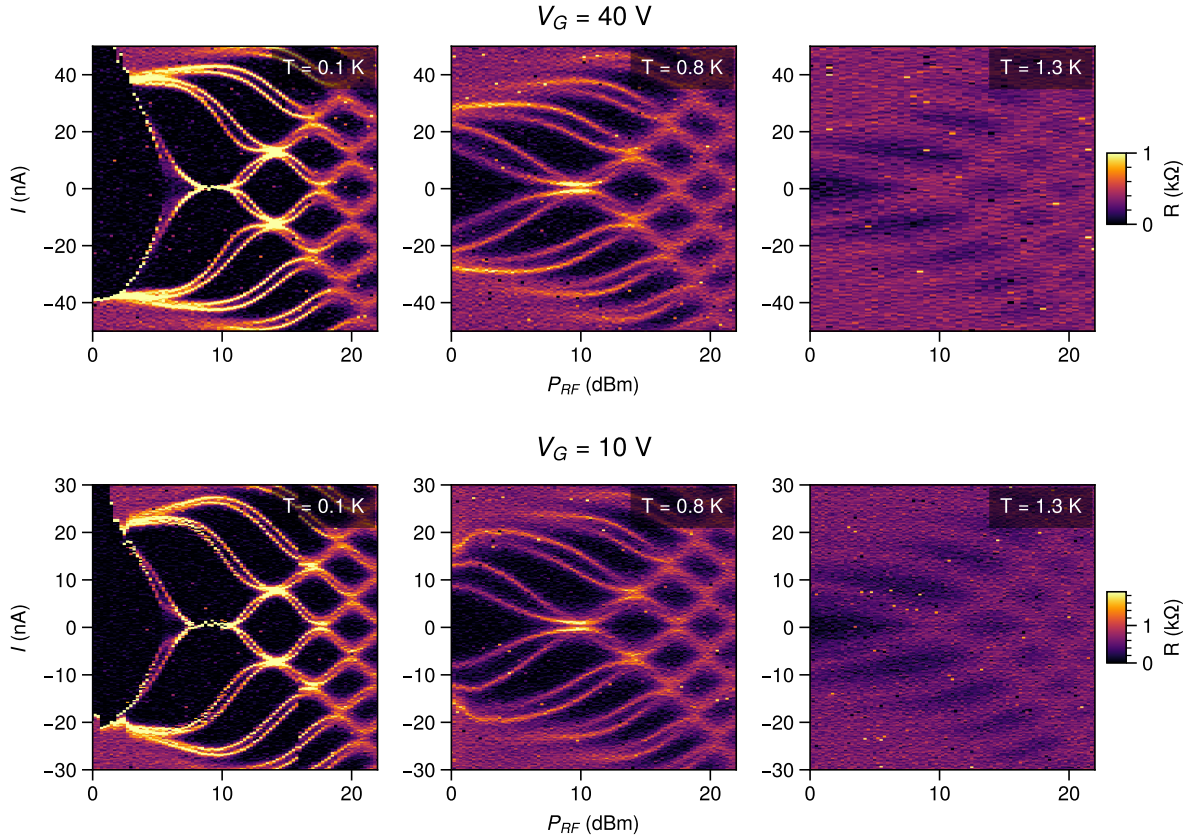


Figure S6: Top row: Shapiro maps at $f = 1.75$ GHz for different temperatures of 0.1 K, 0.8 K, and 1.3 K at a backgate voltage of 40 V. Bottom row: same maps for a backgate voltage of 10 V.

Shapiro Maps at Zero Crossing Step

We present in Fig. S7 a more detailed scan of the Shapiro map at $f = 1.75$ GHz, covering a restricted range of microwave power and currents as shown in Figure 2 of the main text. Zero-crossing steps (red line) are visible as a result of the overlapping ± 1 lobes. The presence

of zero-crossing steps has been extensively investigated in Larson et al.⁴¹ and explained as a consequence of the shunting RC environment and the high $I_c R_j$ product.

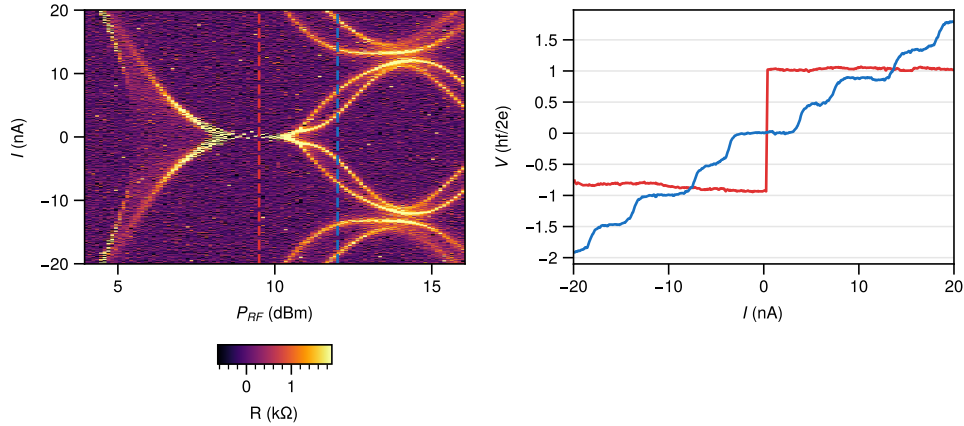


Figure S7: Left: A zoom-in view of the Shapiro maps at $f = 1.75$ GHz, as shown in Figure 2 of the main text, highlighting the zero-crossing steps and providing finer details of the half-integer plateaus. Right: The red and blue $V(I)$ cut shown on the left for $P_{RF} = 9$ dBm and $P_{RF} = 12$ dBm, respectively.

Data from an additional Device with lower Transparency

An additional device has been measured in a similar way, which had a 5 nm Ti adhesion layer embedded under the niobium layer. In this case, only weak signatures of half-integer steps are visible.

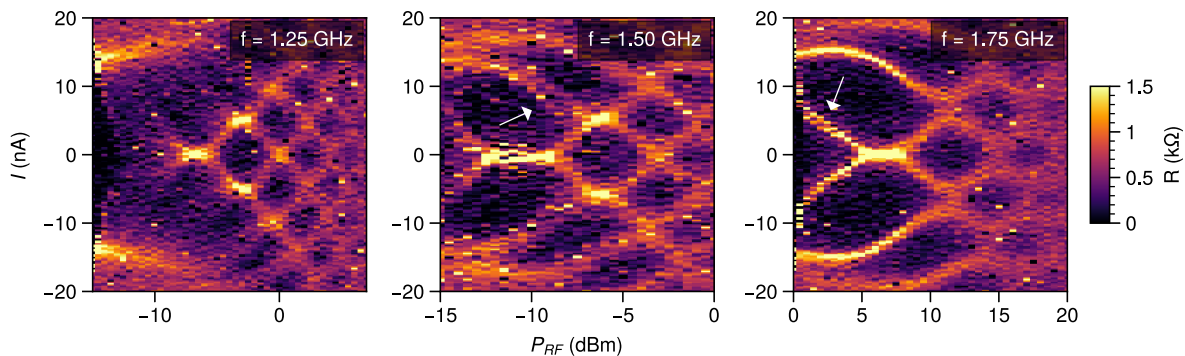


Figure S8: Shapiro maps for $f = 1.25, 1.50$ and 1.75 GHz for a device with reduced transparency.

Theory

CPR under microwave irradiation

Our microscopic model for a microwave-irradiated Josephson junction is based on the works of Cuevas et al.⁹⁰, Bergeret et al.⁹³, Cuevas and Yeyati⁹⁷ and consists of a highly transparent junction, with a short ballistic region between the left and right superconducting leads (L and R, respectively), as schematically displayed in Figure S9a. We describe the system through

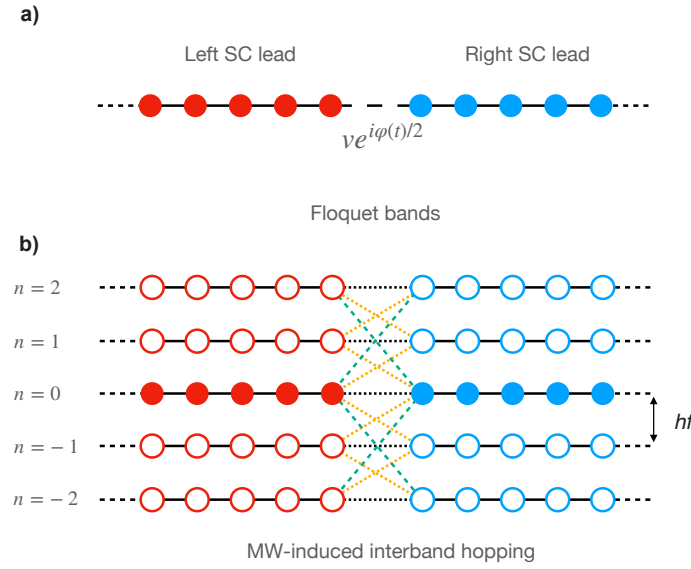


Figure S9: (a) 1D tight-binding model describing the Josephson junction. The driving appears as a time-dependent phase in the left-right hopping amplitude. (b) Floquet side bands shifted in energy by nhf . The different bands are coupled at the interface by the time-oscillating phase.

the 1D tight-binding Hamiltonian $H = H_L + H_R + \sum_{\sigma} (v c_{L\sigma}^{\dagger} c_{R\sigma} + v^* c_{R\sigma}^{\dagger} c_{L\sigma})$, where the left and right leads are described by $H_{\alpha} = -\mu \sum_{n\sigma} c_{\alpha,n,\sigma}^{\dagger} c_{\alpha,n,\sigma} - t \sum_{n,\sigma} (c_{\alpha,\sigma,n}^{\dagger} c_{\alpha,\sigma,n+1} + \text{H.c.}) + \Delta_{\alpha} \sum_n c_{\alpha,n,\uparrow}^{\dagger} c_{\alpha,n,\downarrow}^{\dagger} + \text{H.c.}$, with c and c^{\dagger} being the annihilation/creation operators for particles with spin σ in the superconducting leads and $\Delta_{\alpha} = \Delta e^{i\varphi_{\alpha}}$, with $\varphi_R - \varphi_L = \varphi$ their phase difference. The normal state transmission of this single channel model is $\tau = \frac{4(v/W)^2}{(1+(v/W)^2)^2}$, where $W = 1/(\pi\rho_F) = \sqrt{4t^2 - \mu^2}/2$ and ρ_F is the density of states at the Fermi energy in the leads. The current takes the form $\hat{I}(t) = \frac{ie}{\hbar} \sum_{\sigma} (v c_{L\sigma}^{\dagger} c_{R\sigma} - v^* c_{R\sigma}^{\dagger} c_{L\sigma})$, and under microwave

irradiation, the phase difference acquires the time dependence $\varphi(t) = \varphi_0 + 2w \sin(2\pi ft)$ with $w = eV_{ac}/hf$, so that $v \rightarrow ve^{i\varphi(t)/2}$.

The microwave source can inject and absorb photons of frequency f , so that an incident carrier with energy ϵ can be scattered into states with energy $\epsilon + nhf$. Introducing the Floquet sidebands, which are replicas of the system shifted in energy by nhf , the hopping term \hat{v}_{LR} can couple different sidebands $\hat{v}_{n,m} = \int dt e^{i(n-m)2\pi ft} \hat{v}(t) = v \begin{pmatrix} J_{n-m}(w)e^{i\varphi_0/2} & 0 \\ 0 & -J_{m-n}(w)e^{-i\varphi_0/2} \end{pmatrix}$, where $J_n(w)$ are Bessel functions of the first kind, and we have absorbed the possible phase of v in the phase difference φ_0 . The hopping between the L and R leads acquires a matrix structure that connects the rightmost site in the L lead and Floquet band n with the leftmost site of the R lead and Floquet band m , as schematized in Fig. S9b.

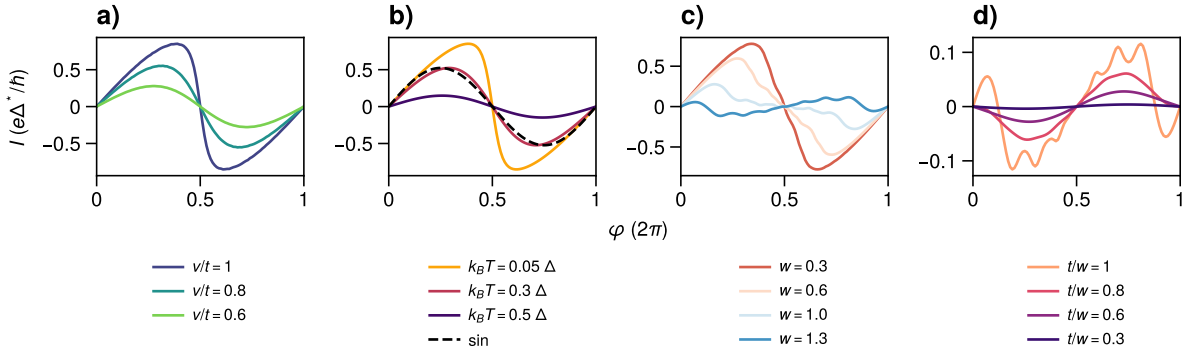


Figure S10: Different CPRs: (a) in the absence of microwave irradiation for different transparencies, (b) in the absence of microwave irradiation for different temperatures, (c) for different microwave drive strengths at $v/t = 1$, and (d) for different transparencies at driving $w = 1.3$.

We now apply the microscopic theory and calculate different CPRs under microwave irradiation. In the absence of driving ($w = 0$), the model accurately reproduced the CPRs of the junction in both the highly transparent and tunneling regimes by varying the ratio v/t , as shown in Fig. S10a, and for different temperatures, as shown in Fig. S10b. We then apply increasing microwave driving and observe a second zero of the CPR in the interval $0-\pi$, along with a region of negative current for positive phase bias, which indicated the occurrence of a secondary minimum (Fig. S10c). At high driving amplitude, the CPR exhibits wiggles due

to the presence of Floquet sidebands, which decay with temperature, as shown in Fig. 3e of the main text. Finally, Figure S10d shows that the CPR loses its secondary zero for low transmission. These features are qualitatively similar to those observed in the additional device reported in the experiment. Including additional bands up to 6 does not qualitatively change the discussion above.

RCSJ model

In the previous section, we described the microscopic theory of non-equilibrium supercurrents in a microwave irradiated Josephson junction in the presence of an AC voltage bias. However, modeling the time-dependent phase dynamics in the presence of non-equilibrium effects, particularly for the experimentally relevant current-bias scenario, is more challenging. Moreover, we find that the environment surrounding the junction plays an important role, as confirmed by the deviations from the Bessel regime and the presence of zero-crossing steps. We opted for a simplistic approach that employs a modified version of the resistively and capacitively shunted junction (RCSJ) model, which includes the dissipative environment surrounding the junction^{3,41} and incorporates the non-equilibrium effects only in a single effective CPR. Despite the simplicity of the assumptions, we are able to capture the main findings of this work. The junction, which has a critical current I_c , is shunted by a capacitance C_j and resistance R_j , and is additionally shunted by an RC environment represented by a parallel capacitor C and resistor R . The entire circuit is biased by a current I , which accounts for the external DC and AC bias. The equations for the current I and the voltage V , shown in Figure 1c, are:

$$\begin{aligned}
 I &= I_{DC} + I_{RF} \sin(2\pi ft) \\
 &= C \frac{dV}{dt} + \text{CPR}(\varphi) + \frac{\hbar}{2eR_j} \frac{d\varphi}{dt} + \frac{\hbar C_j}{2e} \frac{d^2\varphi}{dt^2} \\
 V &= \frac{\hbar}{2e} \frac{d\varphi}{dt} + R \left(\text{CPR}(\varphi) + \frac{\hbar}{2eR_j} \frac{d\varphi}{dt} + \frac{\hbar C_j}{2e} \frac{d^2\varphi}{dt^2} \right),
 \end{aligned} \tag{S1}$$

where φ is the macroscopic phase difference across the junction, I_{DC} and I_{RF} are the DC and RF current biases, respectively, and $\text{CPR}(\varphi)$ is the junction's current-phase relationship. We use a fourth-order Runge-Kutta method to solve for $\varphi(t)$ and obtain the DC voltage across the junction as $V_j = \langle \frac{\hbar}{2e} \frac{d\varphi}{dt} \rangle$.

In the limit of small I_c , the Shapiro map follows the Bessel function dependence, with steps centered at $I_n = \frac{V_n}{R_j}$ and an extension of $\sim I_c |J_n(2w)|$, where $V_n = n \frac{\hbar f}{2e}$ and $w = eV_{AC}/\hbar f$. Figure S11a shows the Shapiro map at lower I_c with an applied external magnetic field of $B = 5$ mT. From the position of the centers, we can extract $R_j \sim 420 \Omega$ (dotted white lines), while the dashed lines show a good agreement with the Bessel behavior, depicting the amplitudes $I_c |J_n(2w)|$, with $V_{AC} = \alpha \times 10^{P_{RF}/20}$, $\alpha \sim 0.8$ and $I_c \sim 10$ nA.

Figures S11b and S11c show the complete maps for the simulation presented in Fig. 3d of the main text for the equilibrium and non-equilibrium CPRs, respectively, obtained by the model in Eq. S1. While the equilibrium CPR well describes the overall trend, it completely lacks half-integer steps, which are instead captured by the effective non-equilibrium CPR. This is despite the presence of higher-order harmonics in the skewed equilibrium CPR. In the simulation, we estimate the geometric capacitance of the junction to be \sim fF and neglect C_j . The capacitance C is determined by the bonding pads' capacitance to the SiO_2 backgate, which we estimate to be $C \sim 15$ pF, while the value of R is set to $R \sim 150 \Omega$ to achieve the best agreement with the experiment. The CPR is expressed as $\text{CPR}(\varphi) = \sum_n I_{c,n} \sin(n\varphi)$, where $I_c = \max_\varphi \text{CPR}(\varphi)$, which is set to 35 nA. The current I_{RF} is given by $I_{RF} = \beta \times 10^{P_{RF}/20}$ with $\beta \sim 20$.

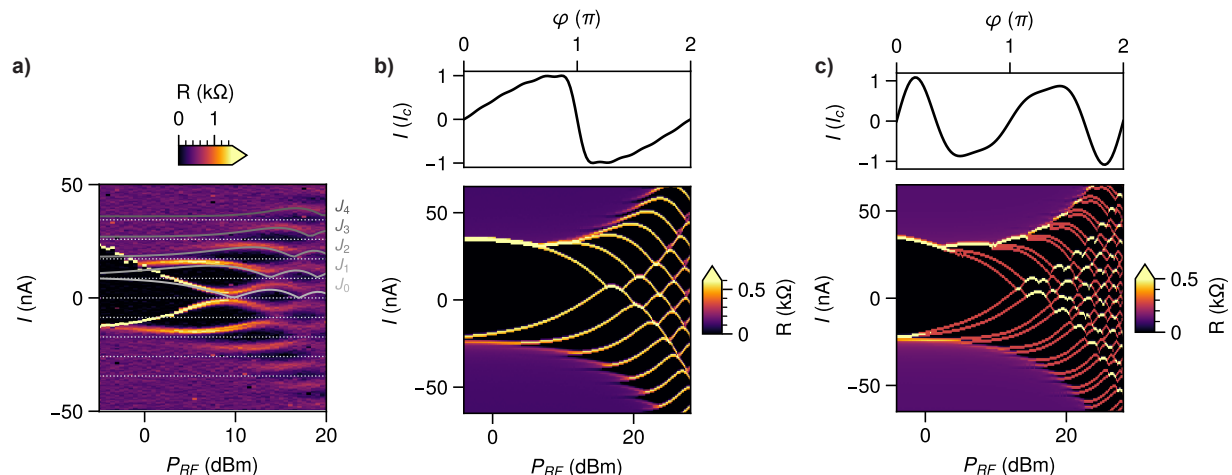


Figure S11: (a) Experimentally measured Shapiro map in the Bessel regime at $B = 5$ mT. The dotted white lines are used to extract R_j , while the continuous lines show the dependence on the Bessel function J_n . (b) Numerical simulation of the Shapiro map with the equilibrium skewed CPR. The amplitudes of the harmonics are $I_{c,n} = (0.91, -0.33, 0.19, -0.12, 0.09, -0.06, 0.04, -0.03, 0.03, -0.02)$. (c) Same as in (b) for the effective non-equilibrium CPR with the amplitudes $I_{c,n} = (-0.38, 0.75, 0.44, 0.22)$.

References

- (1) Kulik, I. O. Macroscopic Quantization and the Proximity Effect in S-N-S Junctions. *Soviet Journal of Experimental and Theoretical Physics* **1969**, *30*, 944.
- (2) Pannetier, B.; Courtois, H. Andreev Reflection and Proximity Effect. *Journal of Low Temperature Physics* **2000**, *118*, 599–615.
- (3) Jarillo-Herrero, P.; van Dam, J. A.; Kouwenhoven, L. P. Quantum Supercurrent Transistors in Carbon Nanotubes. *Nature* **2006**, *439*, 953–956.
- (4) Calado, V. E.; Goswami, S.; Nanda, G.; Diez, M.; Akhmerov, A. R.; Watanabe, K.; Taniguchi, T.; Klapwijk, T. M.; Vandersypen, L. M. K. Ballistic Josephson Junctions in Edge-Contacted Graphene. *Nature Nanotechnology* **2015**, *10*, 761–764.
- (5) Lehnert, K. W.; Argaman, N.; Blank, H.-R.; Wong, K. C.; Allen, S. J.; Hu, E. L.;

- Kroemer, H. Nonequilibrium ac Josephson Effect in Mesoscopic Nb-InAs-Nb Junctions. *Physical Review Letters* **1999**, *82*, 1265–1268.
- (6) Giazotto, F.; Grove-Rasmussen, K.; Fazio, R.; Beltram, F.; Linfield, E. H.; Ritchie, D. A. Josephson Current in Nb/InAs/Nb Highly Transmissive Ballistic Junctions. *Journal of Superconductivity* **2004**, *17*, 317–321.
- (7) Ke, C. T.; Moehle, C. M.; de Vries, F. K.; Thomas, C.; Metti, S.; Guinn, C. R.; Kallaher, R.; Lodari, M.; Scappucci, G.; Wang, T.; Diaz, R. E.; Gardner, G. C.; Manfra, M. J.; Goswami, S. Ballistic Superconductivity and Tunable π -Junctions in InSb Quantum Wells. *Nature Communications* **2019**, *10*, 3764.
- (8) Sellier, H.; Baraduc, C.; Lefloch, F.; Calemczuk, R. Half-Integer Shapiro Steps at the $0 - \pi$ Crossover of a Ferromagnetic Josephson Junction. *Physical Review Letters* **2004**, *92*, 257005.
- (9) Frolov, S. M.; Van Harlingen, D. J.; Bolginov, V. V.; Oboznov, V. A.; Ryazanov, V. V. Josephson Interferometry and Shapiro Step Measurements of Superconductor-Ferromagnet-Superconductor $0 - \pi$ Junctions. *Physical Review B* **2006**, *74*, 020503.
- (10) Veldhorst, M.; Snelder, M.; Hoek, M.; Gang, T.; Guduru, V. K.; Wang, X. L.; Zeitler, U.; van der Wiel, W. G.; Golubov, A. A.; Hilgenkamp, H.; Brinkman, A. Josephson Supercurrent through a Topological Insulator Surface State. *Nature Materials* **2012**, *11*, 417–421.
- (11) Hart, S.; Ren, H.; Wagner, T.; Leubner, P.; Mühlbauer, M.; Brüne, C.; Buhmann, H.; Molenkamp, L. W.; Yacoby, A. Induced Superconductivity in the Quantum Spin Hall Edge. *Nature Physics* **2014**, *10*, 638–643.
- (12) Pribiag, V. S.; Beukman, A. J. A.; Qu, F.; Cassidy, M. C.; Charpentier, C.; Wegscheider, W.; Kouwenhoven, L. P. Edge-Mode Superconductivity in a Two Dimensional Topological Insulator. *Nature Nanotechnology* **2015**, *10*, 593–597.

- (13) Qu, F.; van Veen, J.; de Vries, F. K.; Beukman, A. J. A.; Wimmer, M.; Yi, W.; Kiselev, A. A.; Nguyen, B.-M.; Sokolich, M.; Manfra, M. J.; Nichele, F.; Marcus, C. M.; Kouwenhoven, L. P. Quantized Conductance and Large g -Factor Anisotropy in InSb Quantum Point Contacts. *Nano Letters* **2016**, *16*, 7509–7513.
- (14) Mayer, W.; Schiela, W. F.; Yuan, J.; Hatefipour, M.; Sarney, W. L.; Svensson, S. P.; Leff, A. C.; Campos, T.; Wickramasinghe, K. S.; Dartiailh, M. C.; Žutić, I.; Shabani, J. Superconducting Proximity Effect in InAsSb Surface Quantum Wells with In Situ Al Contacts. *ACS Applied Electronic Materials* **2020**, *2*, 2351–2356.
- (15) Moehle, C. M.; Ke, C. T.; Wang, Q.; Thomas, C.; Xiao, D.; Karwal, S.; Lodari, M.; van de Kerkhof, V.; Termaat, R.; Gardner, G. C.; Scappucci, G.; Manfra, M. J.; Goswami, S. InSbAs Two-Dimensional Electron Gases as a Platform for Topological Superconductivity. *Nano Letters* **2021**, *21*, 9990–9996.
- (16) Lei, Z.; Lehner, C. A.; Cheah, E.; Mittag, C.; Karalic, M.; Wegscheider, W.; Ensslin, K.; Ihn, T. Gate-Defined Quantum Point Contact in an InSb Two-Dimensional Electron Gas. *Physical Review Research* **2021**, *3*, 023042.
- (17) Chen, Y.; Huang, S.; Mu, J.; Pan, D.; Zhao, J.; Xu, H.-Q. A Double Quantum Dot Defined by Top Gates in a Single Crystalline InSb Nanosheet. *Chinese Physics B* **2021**, *30*, 128501.
- (18) de la Mata, M.; Leturcq, R.; Plissard, S. R.; Rolland, C.; Magén, C.; Arbiol, J.; Caroff, P. Twin-Induced InSb Nanosails: A Convenient High Mobility Quantum System. *Nano Letters* **2016**, *16*, 825–833.
- (19) de Vries, F. K.; Sol, M. L.; Gazibegovic, S.; op het Veld, R. L. M.; Balk, S. C.; Car, D.; Bakkers, E. P. A. M.; Kouwenhoven, L. P.; Shen, J. Crossed Andreev Reflection in InSb Flake Josephson Junctions. *Physical Review Research* **2019**, *1*, 032031.

- (20) Pan, D.; Fan, D. X.; Kang, N.; Zhi, J. H.; Yu, X. Z.; Xu, H. Q.; Zhao, J. H. Free-Standing Two-Dimensional Single-Crystalline InSb Nanosheets. *Nano Letters* **2016**, *16*, 834–841.
- (21) Zhi, J.; Kang, N.; Li, S.; Fan, D.; Su, F.; Pan, D.; Zhao, S.; Zhao, J.; Xu, H. Super-current and Multiple Andreev Reflections in InSb Nanosheet SNS Junctions. *physica status solidi (b)* **2019**, *256*, 1800538.
- (22) Zhi, J.; Kang, N.; Su, F.; Fan, D.; Li, S.; Pan, D.; Zhao, S. P.; Zhao, J.; Xu, H. Q. Co-existence of Induced Superconductivity and Quantum Hall States in InSb Nanosheets. *Physical Review B* **2019**, *99*, 245302.
- (23) Verma, I.; Zannier, V.; Rossi, F.; Ercolani, D.; Beltram, F.; Sorba, L. Morphology Control of Single-Crystal InSb Nanostructures by Tuning the Growth Parameters. *Nanotechnology* **2020**, *31*, 384002.
- (24) Kang, N.; Fan, D.; Zhi, J.; Pan, D.; Li, S.; Wang, C.; Guo, J.; Zhao, J.; Xu, H. Two-Dimensional Quantum Transport in Free-Standing InSb Nanosheets. *Nano Letters* **2019**, *19*, 561–569.
- (25) Xue, J.; Chen, Y.; Pan, D.; Wang, J.-Y.; Zhao, J.; Huang, S.; Xu, H. Q. Gate Defined Quantum Dot Realized in a Single Crystalline InSb Nanosheet. *Applied Physics Letters* **2019**, *114*, 023108.
- (26) Chen, Y.; Huang, S.; Pan, D.; Xue, J.; Zhang, L.; Zhao, J.; Xu, H. Q. Strong and Tunable Spin-Orbit Interaction in a Single Crystalline InSb Nanosheet. *npj 2D Materials and Applications* **2021**, *5*, 1–8.
- (27) Gazibegovic, S.; Badawy, G.; Buckers, T. L. J.; Leubner, P.; Shen, J.; de Vries, F. K.; Koelling, S.; Kouwenhoven, L. P.; Verheijen, M. A.; Bakkers, E. P. A. M. Bottom-Up Grown 2D InSb Nanostructures. *Advanced Materials* **2019**, *31*, 1808181.

- (28) Verma, I.; Salimian, S.; Zannier, V.; Heun, S.; Rossi, F.; Ercolani, D.; Beltram, F.; Sorba, L. High-Mobility Free-Standing InSb Nanoflags Grown on InP Nanowire Stems for Quantum Devices. *ACS Applied Nano Materials* **2021**, *4*, 5825–5833.
- (29) Rossi, M.; Badawy, G.; Zhang, Z.-Y.; Yang, G.; Li, G.-A.; Shi, J.-Y.; Op het Veld, R. L. M.; Gazibegovic, S.; Li, L.; Shen, J.; Verheijen, M. A.; Bakkers, E. P. A. M. Merging Nanowires and Formation Dynamics of Bottom-Up Grown InSb Nanoflakes. *Advanced Functional Materials* *n/a*, 2212029.
- (30) Salimian, S.; Carrega, M.; Verma, I.; Zannier, V.; Nowak, M. P.; Beltram, F.; Sorba, L.; Heun, S. Gate-Controlled Supercurrent in Ballistic InSb Nanoflag Josephson Junctions. *Applied Physics Letters* **2021**, *119*, 214004.
- (31) Turini, B.; Salimian, S.; Carrega, M.; Iorio, A.; Strambini, E.; Giazotto, F.; Zannier, V.; Sorba, L.; Heun, S. Josephson Diode Effect in High-Mobility InSb Nanoflags. *Nano Letters* **2022**,
- (32) Fornieri, A. et al. Evidence of Topological Superconductivity in Planar Josephson Junctions. *Nature* **2019**, *569*, 89–92.
- (33) Prada, E.; San-Jose, P.; de Moor, M. W. A.; Geresdi, A.; Lee, E. J. H.; Klinovaja, J.; Loss, D.; Nygård, J.; Aguado, R.; Kouwenhoven, L. P. From Andreev to Majorana Bound States in Hybrid Superconductor–Semiconductor Nanowires. *Nature Reviews Physics* **2020**, *2*, 575–594.
- (34) Larsen, T. W.; Petersson, K. D.; Kuemmeth, F.; Jespersen, T. S.; Krogstrup, P.; Nygård, J.; Marcus, C. M. Semiconductor-Nanowire-Based Superconducting Qubit. *Physical Review Letters* **2015**, *115*, 127001.
- (35) Casparis, L.; Connolly, M. R.; Kjaergaard, M.; Pearson, N. J.; Kringhøj, A.; Larsen, T. W.; Kuemmeth, F.; Wang, T.; Thomas, C.; Gronin, S.; Gardner, G. C.;

- Manfra, M. J.; Marcus, C. M.; Petersson, K. D. Superconducting Gatemon Qubit Based on a Proximitized Two-Dimensional Electron Gas. *Nature Nanotechnology* **2018**, *13*, 915–919.
- (36) Hays, M.; Fatemi, V.; Bouman, D.; Cerrillo, J.; Diamond, S.; Serniak, K.; Connolly, T.; Krogstrup, P.; Nygård, J.; Levy Yeyati, A.; Geresdi, A.; Devoret, M. H. Coherent Manipulation of an Andreev Spin Qubit. *Science* **2021**, *373*, 430–433.
- (37) Basset, J.; Kuzmanović, M.; Virtanen, P.; Heikkilä, T. T.; Estève, J.; Gabelli, J.; Strunk, C.; Aprili, M. Nonadiabatic Dynamics in Strongly Driven Diffusive Josephson Junctions. *Physical Review Research* **2019**, *1*, 032009.
- (38) Catelani, G.; Basko, D. Non-Equilibrium Quasiparticles in Superconducting Circuits: Photons vs. Phonons. *SciPost Physics* **2019**, *6*, 013.
- (39) Kjaergaard, M.; Suominen, H. J.; Nowak, M. P.; Akhmerov, A. R.; Shabani, J.; Palmstrøm, C. J.; Nichele, F.; Marcus, C. M. Transparent Semiconductor-Superconductor Interface and Induced Gap in an Epitaxial Heterostructure Josephson Junction. *Physical Review Applied* **2017**, *7*, 034029.
- (40) Russer, P. Influence of Microwave Radiation on Current-Voltage Characteristic of Superconducting Weak Links. *Journal of Applied Physics* **1972**, *43*, 2008–2010.
- (41) Larson, T. F. Q.; Zhao, L.; Arnault, E. G.; Wei, M.-T.; Serebinski, A.; Li, H.; Watanabe, K.; Taniguchi, T.; Amet, F.; Finkelstein, G. Zero Crossing Steps and Anomalous Shapiro Maps in Graphene Josephson Junctions. *Nano Letters* **2020**, *20*, 6998–7003.
- (42) Courtois, H.; Meschke, M.; Peltonen, J. T.; Pekola, J. P. Origin of Hysteresis in a Proximity Josephson Junction. *Physical Review Letters* **2008**, *101*, 067002.
- (43) Antonenko, D. S.; Skvortsov, M. A. Quantum Decay of the Supercurrent and Intrinsic

- Capacitance of Josephson Junctions beyond the Tunnel Limit. *Physical Review B* **2015**, *92*, 214513.
- (44) Massarotti, D.; Banerjee, N.; Caruso, R.; Rotoli, G.; Blamire, M. G.; Tafuri, F. Electrodynamics of Josephson Junctions Containing Strong Ferromagnets. *Physical Review B* **2018**, *98*, 144516.
- (45) Fischer, R.; Picó-Cortés, J.; Himmler, W.; Platero, G.; Grifoni, M.; Kozlov, D. A.; Mikhailov, N. N.; Dvoretzky, S. A.; Strunk, C.; Weiss, D. 4π -Periodic Supercurrent Tuned by an Axial Magnetic Flux in Topological Insulator Nanowires. *Physical Review Research* **2022**, *4*, 013087.
- (46) Beenakker, C. W. J. Universal Limit of Critical-Current Fluctuations in Mesoscopic Josephson Junctions. *Physical Review Letters* **1991**, *67*, 3836–3839.
- (47) Mühlischlegel, B. Die thermodynamischen Funktionen des Supraleiters. *Zeitschrift für Physik* **1959**, *155*, 313–327.
- (48) Dubos, P.; Courtois, H.; Pannetier, B.; Wilhelm, F. K.; Zaikin, A. D.; Schön, G. Josephson Critical Current in a Long Mesoscopic S-N-S Junction. *Physical Review B* **2001**, *63*, 064502.
- (49) Borzenets, I. V.; Amet, F.; Ke, C. T.; Draelos, A. W.; Wei, M. T.; Seredinski, A.; Watanabe, K.; Taniguchi, T.; Bomze, Y.; Yamamoto, M.; Tarucha, S.; Finkelstein, G. Ballistic Graphene Josephson Junctions from the Short to the Long Junction Regimes. *Physical Review Letters* **2016**, *117*, 237002.
- (50) Kayyalha, M.; Kargarian, M.; Kazakov, A.; Miotkowski, I.; Galitski, V. M.; Yakovenko, V. M.; Rokhinson, L. P.; Chen, Y. P. Anomalous Low-Temperature Enhancement of Supercurrent in Topological-Insulator Nanoribbon Josephson Junctions: Evidence for Low-Energy Andreev Bound States. *Physical Review Letters* **2019**, *122*, 047003.

- (51) Schüffelgen, P. et al. Selective Area Growth and Stencil Lithography for in Situ Fabricated Quantum Devices. *Nature Nanotechnology* **2019**, *14*, 825–831.
- (52) Stolyarov, V. S. et al. Josephson Current Mediated by Ballistic Topological States in $\text{Bi}_2\text{Te}_{2.3}\text{Se}_{0.7}$ Single Nanocrystals. *Communications Materials* **2020**, *1*, 1–11.
- (53) Rosenbach, D.; Schmitt, T. W.; Schüffelgen, P.; Stehno, M. P.; Li, C.; Schleenvoigt, M.; Jalil, A. R.; Mussler, G.; Neumann, E.; Trelenkamp, S.; Golubov, A. A.; Brinkman, A.; Grützmacher, D.; Schäpers, T. Reappearance of First Shapiro Step in Narrow Topological Josephson Junctions. *Science Advances* **2021**, *7*, eabf1854.
- (54) Schmitt, T. W.; Frohn, B.; Wittl, W.; Jalil, A. R.; Schleenvoigt, M.; Zimmermann, E.; Schmidt, A.; Schäpers, T.; Cuevas, J. C.; Brinkman, A.; Grützmacher, D.; Schüffelgen, P. Anomalous Temperature Dependence of Multiple Andreev Reflections in a Topological Insulator Josephson Junction. *Superconductor Science and Technology* **2022**, *36*, 024002.
- (55) Barzykin, V.; Zagoskin, A. M. Coherent Transport and Nonlocality in Mesoscopic SNS Junctions: Anomalous Magnetic Interference Patterns. *Superlattices and Microstructures* **1999**, *25*, 797–807.
- (56) Cuevas, J. C.; Bergeret, F. S. Magnetic Interference Patterns and Vortices in Diffusive SNS Junctions. *Physical Review Letters* **2007**, *99*, 217002.
- (57) Angers, L.; Chiodi, F.; Montambaux, G.; Ferrier, M.; Guéron, S.; Bouchiat, H.; Cuevas, J. C. Proximity dc Squids in the Long-Junction Limit. *Physical Review B* **2008**, *77*, 165408.
- (58) Chiodi, F.; Ferrier, M.; Guéron, S.; Cuevas, J. C.; Montambaux, G.; Fortuna, F.; Kasumov, A.; Bouchiat, H. Geometry-Related Magnetic Interference Patterns in Long SNS Josephson Junctions. *Physical Review B* **2012**, *86*, 064510.

- (59) Blom, T. J.; Mechielsen, T. W.; Fermin, R.; Hesselberth, M. B. S.; Aarts, J.; Lahabi, K. Direct-Write Printing of Josephson Junctions in a Scanning Electron Microscope. *ACS Nano* **2021**, *15*, 322–329.
- (60) Gubin, A. I.; Il'in, K. S.; Vitusevich, S. A.; Siegel, M.; Klein, N. Dependence of Magnetic Penetration Depth on the Thickness of Superconducting Nb Thin Films. *Physical Review B* **2005**, *72*, 064503.
- (61) Shapiro, S. Josephson Currents in Superconducting Tunneling: The Effect of Microwaves and Other Observations. *Physical Review Letters* **1963**, *11*, 80–82.
- (62) Zaikin, A. D. Nonstationary Josephson Effect and Nonequilibrium Properties of SNS Junctions. *Zh. Eksp. Teor. Fiz* **1983**, *84*, 1560–1573.
- (63) Argaman, N. Nonequilibrium Josephson-like Effects in Wide Mesoscopic SNS Junctions. *Superlattices and Microstructures* **1999**, *25*, 861–875.
- (64) Dubos, P.; Courtois, H.; Buisson, O.; Pannetier, B. Coherent Low-Energy Charge Transport in a Diffusive S-N-S Junction. *Physical Review Letters* **2001**, *87*, 206801.
- (65) Fuechsle, M.; Bentner, J.; Ryndyk, D. A.; Reinwald, M.; Wegscheider, W.; Strunk, C. Effect of Microwaves on the Current-Phase Relation of Superconductor–Normal-Metal–Superconductor Josephson Junctions. *Physical Review Letters* **2009**, *102*, 127001.
- (66) Dassonneville, B.; Murani, A.; Ferrier, M.; Guéron, S.; Bouchiat, H. Coherence-Enhanced Phase-Dependent Dissipation in Long SNS Josephson Junctions: Revealing Andreev Bound State Dynamics. *Physical Review B* **2018**, *97*, 184505.
- (67) Ueda, K.; Matsuo, S.; Kamata, H.; Sato, Y.; Takeshige, Y.; Li, K.; Samuelson, L.; Xu, H.; Tarucha, S. Evidence of Half-Integer Shapiro Steps Originated from Nonsinu-

- soidal Current Phase Relation in a Short Ballistic InAs Nanowire Josephson Junction. *Physical Review Research* **2020**, *2*, 033435.
- (68) Pfeiffer, J.; Kemmler, M.; Koelle, D.; Kleiner, R.; Goldobin, E.; Weides, M.; Feofanov, A. K.; Lisenfeld, J.; Ustinov, A. V. Static and Dynamic Properties of 0 , π , and $0-\pi$ Ferromagnetic Josephson Tunnel Junctions. *Physical Review B* **2008**, *77*, 214506.
- (69) Stoutimore, M. J. A.; Rossolenko, A. N.; Bolginov, V. V.; Oboznov, V. A.; Rusanov, A. Y.; Baranov, D. S.; Pugach, N.; Frolov, S. M.; Ryazanov, V. V.; Van Harlingen, D. J. Second-Harmonic Current-Phase Relation in Josephson Junctions with Ferromagnetic Barriers. *Physical Review Letters* **2018**, *121*, 177702.
- (70) Shvetsov, O. O.; Kononov, A.; Timonina, A. V.; Kolesnikov, N. N.; Deviatov, E. V. Subharmonic Shapiro Steps in the a.c. Josephson Effect for a Three-Dimensional Weyl Semimetal WTe_2 . *EPL (Europhysics Letters)* **2018**, *124*, 47003.
- (71) Trimble, C. J.; Wei, M. T.; Yuan, N. F. Q.; Kalantre, S. S.; Liu, P.; Han, H.-J.; Han, M.-G.; Zhu, Y.; Cha, J. J.; Fu, L.; Williams, J. R. Josephson Detection of Time-Reversal Symmetry Broken Superconductivity in SnTe Nanowires. *npj Quantum Materials* **2021**, *6*, 1–6.
- (72) Eckern, U.; Schön, G.; Ambegaokar, V. Quantum Dynamics of a Superconducting Tunnel Junction. *Physical Review B* **1984**, *30*, 6419–6431.
- (73) Hamilton, C.; Johnson, E. Analog Computer Studies of Subharmonic Steps in Superconducting Weak Links. *Physics Letters A* **1972**, *41*, 393–394.
- (74) Larson, T. F. Q.; Zhao, L.; Arnault, E. G.; Wei, M.-T.; Serebinski, A.; Li, H.; Watanabe, K.; Tanaguchi, T.; Amet, F.; Finkelstein, G. Noise-induced stabilization of dynamical states in a non-Markovian system. 2022; <https://arxiv.org/abs/2212.13952>.

- (75) Lee, K.; Stroud, D.; Chung, J. Calculation of Giant Fractional Shapiro Steps in Josephson-junction Arrays. *Physical Review Letters* **1990**, *64*, 962–965.
- (76) Lee, H. C.; Newrock, R. S.; Mast, D. B.; Hebboul, S. E.; Garland, J. C.; Lobb, C. J. Subharmonic Shapiro Steps in Josephson-junction Arrays. *Physical Review B* **1991**, *44*, 921–924.
- (77) Heinz, E.; Seidel, P. Microwave-Induced Steps in Josephson Junctions, DC-SQUIDS and Parallel Arrays. *Journal of Low Temperature Physics* **1997**, *106*, 233–242.
- (78) Valizadeh, A.; Kolahchi, M. R.; Straley, J. P. Fractional Shapiro Steps in a Triangular Single-Plaquette Josephson-junction Array. *Physical Review B* **2007**, *76*, 214511.
- (79) Pangotra, R.; Raes, B.; de Souza Silva, C. C.; Cools, I.; Keijers, W.; Scheerder, J. E.; Moshchalkov, V. V.; Van de Vondel, J. Giant Fractional Shapiro Steps in Anisotropic Josephson Junction Arrays. *Communications Physics* **2020**, *3*, 1–8.
- (80) Amet, F.; Idris, S.; McConnell, A.; Opatosky, B.; Arnault, E. Phase Dynamics in an AC-driven Multiterminal Josephson Junction Analog. *Physical Review B* **2022**, *106*, 174509.
- (81) Vanneste, C.; Chi, C. C.; Gallagher, W. J.; Kleinsasser, A. W.; Raider, S. I.; Sandstrom, R. L. Shapiro Steps on Current-voltage Curves of dc SQUIDS. *Journal of Applied Physics* **1988**, *64*, 242–245.
- (82) Early, E. A.; Clark, A. F.; Lobb, C. J. Physical Basis for Half-Integral Shapiro Steps in a DC SQUID. *Physica C: Superconductivity* **1995**, *245*, 308–320.
- (83) Early, E. A.; Clark, A. F.; Char, K. Half-integral Constant Voltage Steps in High- T_c Grain Boundary Junctions. *Applied Physics Letters* **1993**, *62*, 3357–3359.
- (84) Terpstra, D.; IJsselsteijn, R. P. J.; Rogalla, H. Subharmonic Shapiro Steps in High- T_c Josephson Junctions. *Applied Physics Letters* **1995**, *66*, 2286–2288.

- (85) Ku, L. C.; Cho, H. M.; Wang, S. W. The Origin of the Half-Integral Constant Voltage Steps in High- T_c Grain-Boundary Junction. *Physica C: Superconductivity* **1995**, *243*, 187–190.
- (86) Yang, H. C.; Ku, L. C.; Cho, H. M.; Lu, J. H.; Horng, H. E. Observation of Half-Integer Shapiro Steps in Step-Edge $\text{YBa}_2\text{Cu}_3\text{O}_y$ Josephson Junctions. *Physica C: Superconductivity* **1994**, *235–240*, 3341–3342.
- (87) Kroemer, H. Quasiparticle Dynamics in Ballistic Weak Links under Weak Voltage Bias: An Elementary Treatment. *Superlattices and Microstructures* **1999**, *25*, 877–889.
- (88) Biedermann, K.; Chrestin, A.; Matsuyama, T.; Merkt, U. ac Josephson Effects in Nb/InAs/Nb Junctions with Integrated Resonators. *Physical Review B* **2001**, *63*, 144512.
- (89) Baselmans, J. J. A.; Heikkilä, T. T.; van Wees, B. J.; Klapwijk, T. M. Direct Observation of the Transition from the Conventional Superconducting State to the π State in a Controllable Josephson Junction. *Physical Review Letters* **2002**, *89*, 207002.
- (90) Cuevas, J. C.; Heurich, J.; Martín-Rodero, A.; Levy Yeyati, A.; Schön, G. Subharmonic Shapiro Steps and Assisted Tunneling in Superconducting Point Contacts. *Physical Review Letters* **2002**, *88*, 157001.
- (91) Jacobs, A.; Kümmel, R. Andreev Scattering, Zener Tunneling, and Anomalous ac Josephson Effect in near-Ballistic Quasi-Two-Dimensional Weak Links. *Physical Review B* **2005**, *71*, 184504.
- (92) Virtanen, P.; Heikkilä, T. T.; Bergeret, F. S.; Cuevas, J. C. Theory of Microwave-Assisted Supercurrent in Diffusive SNS Junctions. *Physical Review Letters* **2010**, *104*, 247003.

- (93) Bergeret, F. S.; Virtanen, P.; Ozaeta, A.; Heikkilä, T. T.; Cuevas, J. C. Supercurrent and Andreev Bound State Dynamics in Superconducting Quantum Point Contacts under Microwave Irradiation. *Physical Review B* **2011**, *84*, 054504.
- (94) Haxell, D. Z.; Coraiola, M.; Sabonis, D.; Hinderling, M.; Kate, S. C. t.; Cheah, E.; Krizek, F.; Schott, R.; Wegscheider, W.; Belzig, W.; Cuevas, J. C.; Nichele, F. Microwave-induced conductance replicas in hybrid Josephson junctions without Floquet-Andreev states. 2022; <https://arxiv.org/abs/2212.03554>.
- (95) Dou, Z.; Wakamura, T.; Virtanen, P.; Wu, N.-J.; Deblock, R.; Autier-Laurent, S.; Watanabe, K.; Taniguchi, T.; Guéron, S.; Bouchiat, H.; Ferrier, M. Microwave Photoassisted Dissipation and Supercurrent of a Phase-Biased Graphene-Superconductor Ring. *Physical Review Research* **2021**, *3*, L032009.
- (96) Flensberg, K.; Hansen, J. B.; Octavio, M. Subharmonic Energy-Gap Structure in Superconducting Weak Links. *Physical Review B* **1988**, *38*, 8707–8711.
- (97) Cuevas, J. C.; Yeyati, A. L. Subharmonic Gap Structure in Short Ballistic Graphene Junctions. *Physical Review B* **2006**, *74*, 180501.

Graphical TOC Entry

